nature nanotechnology

SUPPLEMENTARY INFORMATION

https://doi.org/10.1038/s41565-018-0096-0

In the format provided by the authors and unedited.

Plasmon-induced carrier polarization in semiconductor nanocrystals

Penghui Yin, Yi Tan, Hanbing Fang, Manu Hegde and Pavle V. Radovanovic*

Department of Chemistry, University of Waterloo, Waterloo, ON, Canada. *e-mail: pavler@uwaterloo.ca

Supplementary Information

Plasmon-induced carrier polarization in semiconductor nanocrystals

Penghui Yin, Yi Tan, Hanbing Fang, Manu Hegde and Pavle V. Radovanovic*

* Email: pavler@uwaterloo.ca

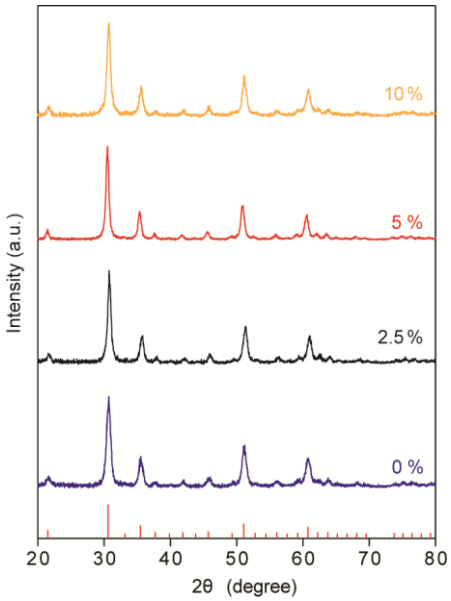

Supplementary Fig. 1. X-ray diffraction patterns of ITO nanocrystals. X-ray diffraction patterns of nanocrystals with different Sn^{4+} doping concentrations, as indicated in the graph. Vertical red lines represent the pattern of bulk cubic (bixbyite) In_2O_3 (JCPDS 06-0416).

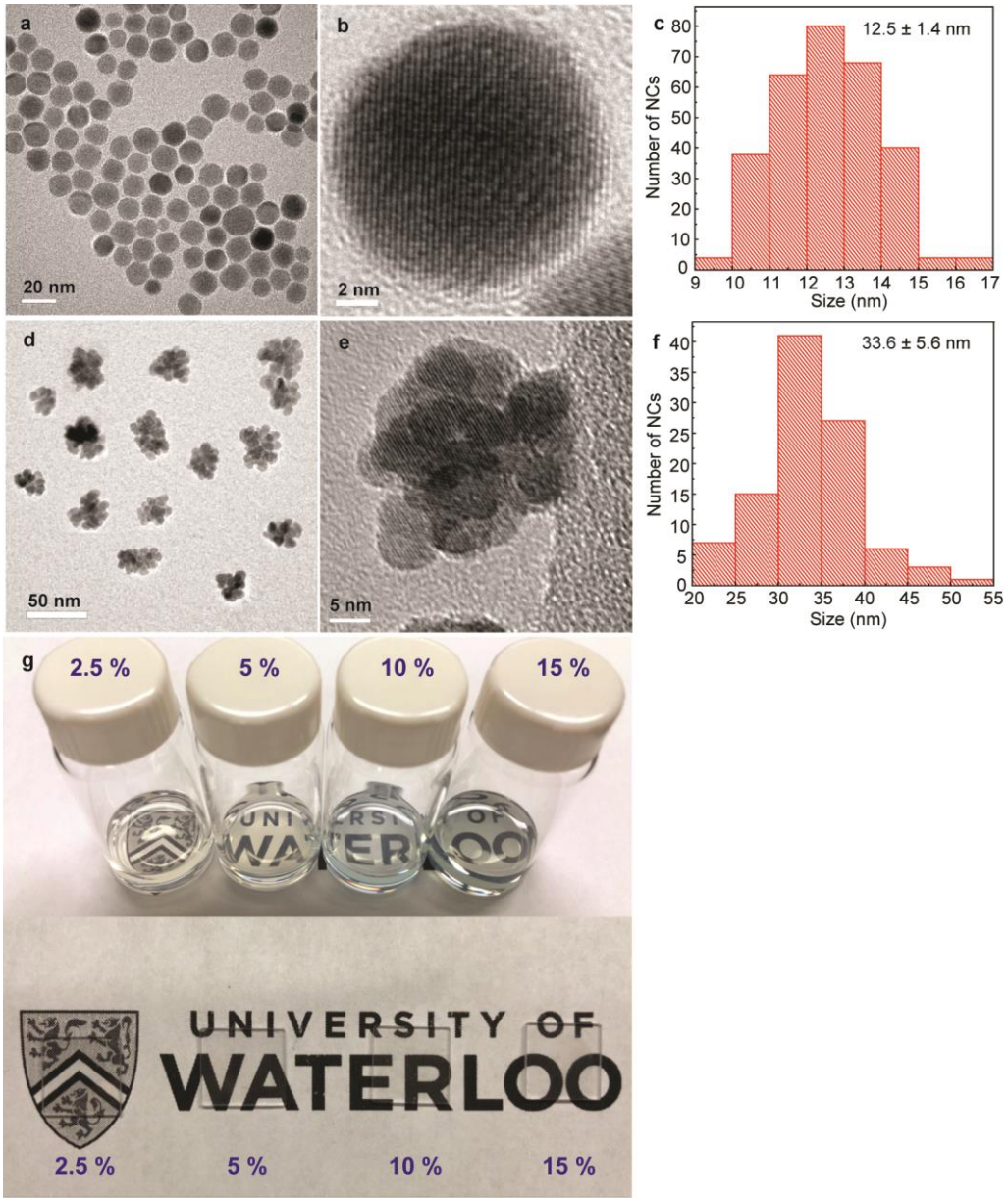

Supplementary Fig 2. Size and morphology of ITO nanocrystals. a-c, Overview transmission electron microscopy (TEM) image (**a**), high-resolution TEM image (**b**), and size distribution histogram (**c**) of ITO nanocrystals with 2.5 % Sn^{4+} doping concentration. **d-f,** Overview TEM image (**d**), high-resolution TEM image (**e**), and size distribution histogram (**f**) of ITO nanocrystals with 10 % Sn^{4+} doping concentration. TEM images of ITO nanocrystals containing 10 % Sn^{4+} show the formation of flower-like clusters, as described elsewhere (ref. 3). ITO nanocrystals were synthesized using $SnCl_4 \cdot 5H_2O$ as a dopant precursor. Chloride ions can replace organic ligands on nanocrystal surfaces,

which reduces their protection. At the same time uneven adsorption of Cl^- ions on different surfaces leads to the formation of a local dipole moment which causes van der Waals interactions and assembly of nanocrystals into uniform flower-like structure by oriented attachment. Lattice-resolved TEM images of a nanoflower in **e** confirms the oriented attachment of nanocrystals within the cluster. The measured average lattice spacing of 2.92 Å matches {222} d-spacing of bixbyite-type In_2O_3. **g,** Photographs of the ITO nanocrystal samples having different Sn^{4+} doping concentration (as indicated in the photograph) in colloidal form (top) and deposited on quartz substrates for MCD measurements (bottom). Both colloidal suspensions and deposited films are completely transparent.

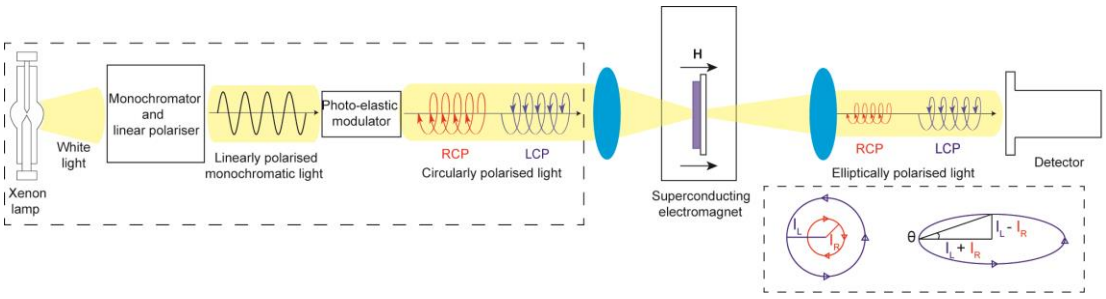

Supplementary Fig 3. Magnetic circular dichroism experimental set-up. A light from a broad-band emitting source is passed through a monochromator and polarizer to generate a monochromatic linearly polarized beam. A portion of this beam is passed through a photoelastic modulator creating left circularly polarized (LCP) and right circularly polarized (RCP) light. A sample is mounted in a superconducting magneto-optical cryostat with the lines of the magnetic field oriented parallel to the light propagation direction. Upon passing through the sample LCP and RCP light are absorbed to a different degree. Different intensities of left and right circularly polarized light (I_L and I_R, respectively) are combined to form an elliptically polarized beam. The ellipticity, θ, is defined as the angle between the long and short axes of the ellipse, and is converted to a differential absorption using eq. 3 in Methods.

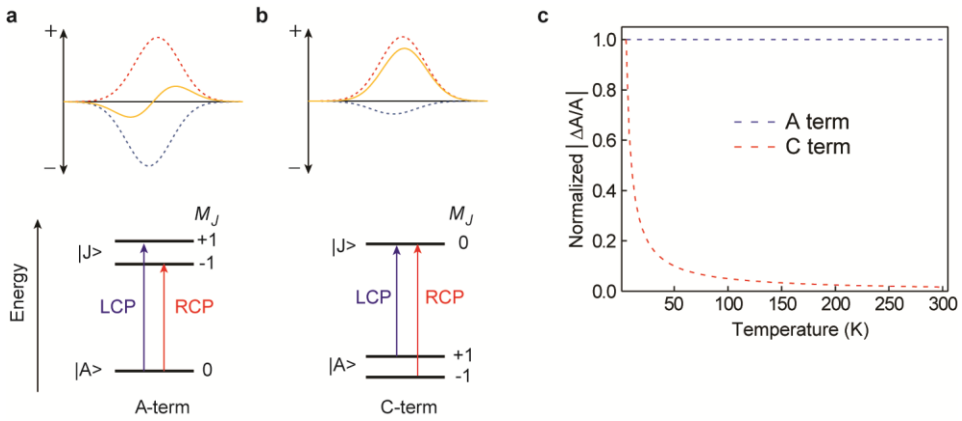

Supplementary Fig 4. Schematic representation of magnetic circular dichroism (MCD) terms. a, MCD signal (top) and Zeeman splitting (bottom) for A-term MCD. A-term is typically associated with Zeeman splitting of the degenerate excited states, as shown in the bottom part. The small Zeeman splitting results in oppositely signed absorption bands for LCP and RCP light (blue and red dashed lines, respectively), which are slightly shifted in energy relative to each other leading to the derivative-shaped MCD signal (yellow line); **b,** MCD signal (top) and Zeeman splitting (bottom) for the C-term MCD. Unlike A-term, C-term involves Zeeman splitting of the degenerate ground states (bottom part). The population of the higher energy ground state is usually lower, and in the absence of excited state splitting the difference in absorption of LCP and RCP light (blue and red dashed lines, respectively) leads to MCD signal with absorption band shape (yellow line); **c,** Comparison of the temperature-dependent A-term and C-term MCD intensity. A-term is temperature independent, while C-term, which is observed only for molecules with ground state paramagnetism, follows Curie-type behaviour.

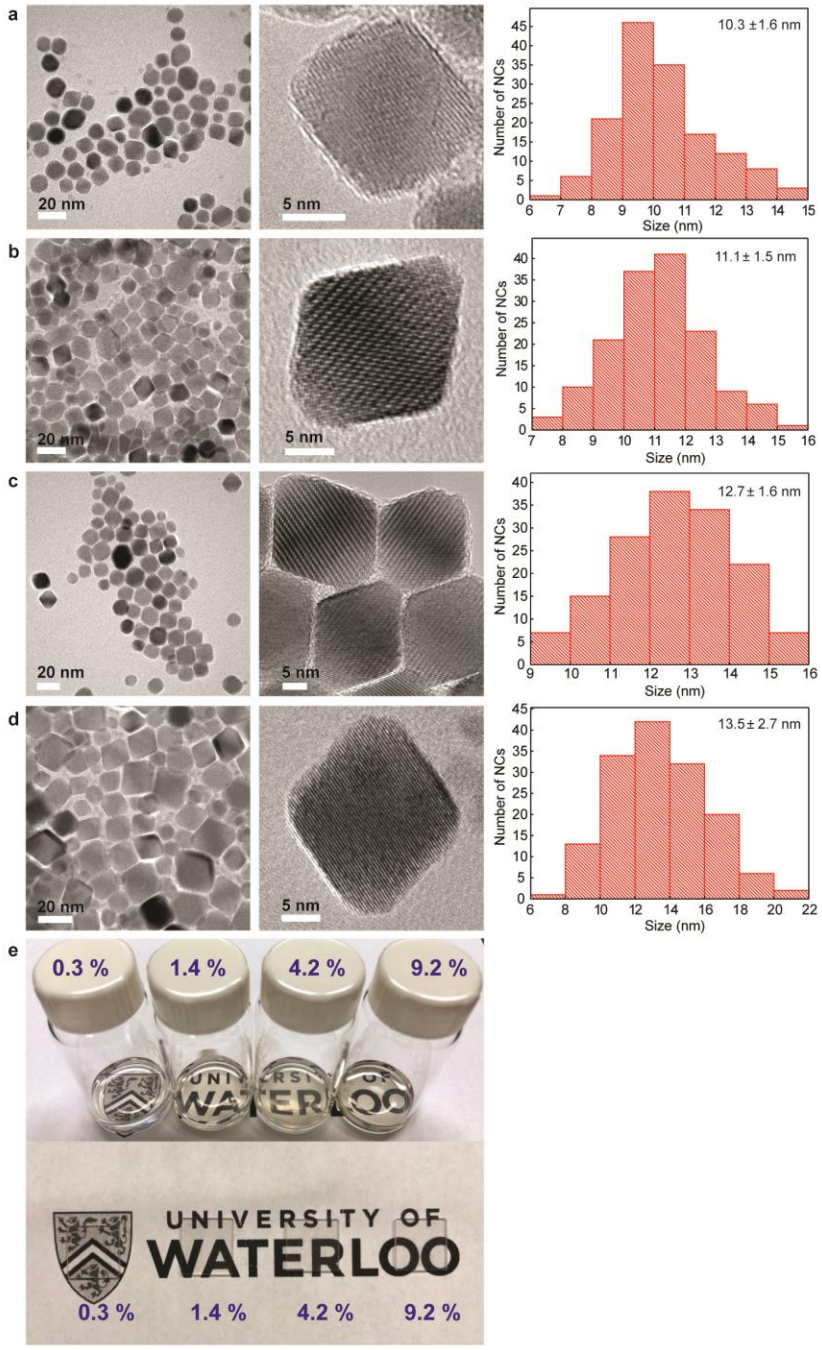

Supplementary Fig 5. Transmission electron microscopy (TEM) images of IMO nanocrystals. a-d, Overview TEM images (left panels), high-resolution TEM images (middle panels) and size distribution histograms (right panels) of IMO nanocrystals with (**a**) 0.3 %, (**b**) 1.4 %, (**c**) 4.2 %, and (**d**) 9.2 % Mo doping concentrations. Average nanocrystal sizes are shown as insets. **e,** Photographs of the same nanocrystal samples in colloidal form (top) and deposited on quartz substrates for MCD measurements (bottom).

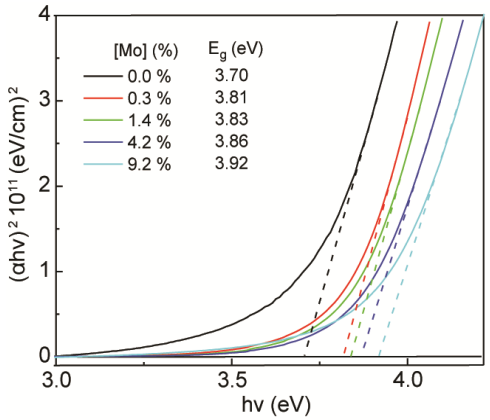

Supplementary Fig 6. Burstein-Moss shift for IMO nanocrystals. Band edge absorption spectra of nanocrystals in Fig. 3b used to determine optical bandgaps by linear extrapolation (Tauc plots). Bandgap energies determined from the extrapolation are shown in the inset. With increasing Mo doping concentration the apparent NC band-edge shifts to higher energy owing to the increased occupancy of conduction band states.

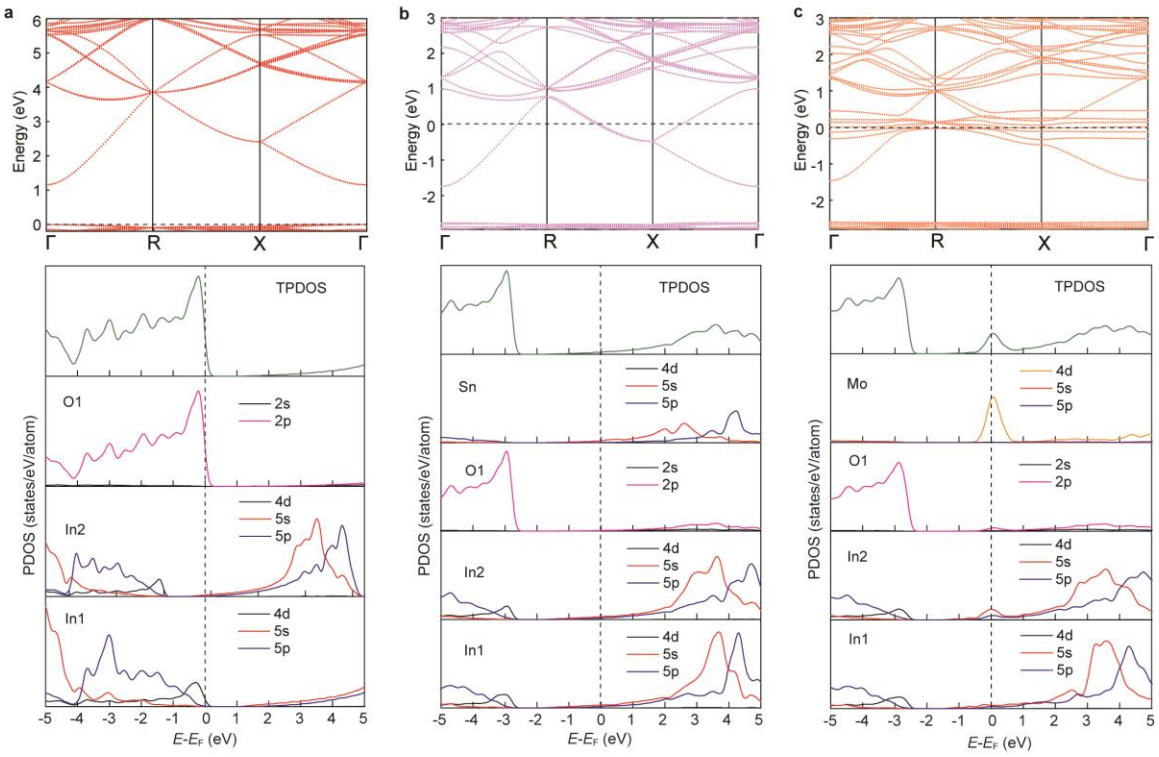

Supplementary Fig 7. Density functional theory (DFT) calculations for undoped and doped In_2O_3. Band structure (top) and projected density of states (bottom) diagrams of (a) In_2O_3, (b) 6.25 % Sn-doped In_2O_3 (ITO), and (c) 6.25 % Mo-doped In_2O_3 (IMO). The Fermi levels are shown with dashed lines. As previously shown (ref. 5 in the main text), band structure diagram confirms that In_2O_3 is a direct bandgap semiconductor, with the valence band maximum and the conduction band minimum at the centre of the Brillouin zone. The calculated bandgap energy at Γ point is ca. 1.15 eV. This value is smaller than optically determined bandgap energy, due to well-documented underestimation of the band gap energy by DFT[S1]. The conduction band has a large dispersion, indicating a low effective electron mass and high electron mobility[S2]. The band structure diagram for ITO also shows large conduction band dispersion and the low effective electron mass, similarly to In_2O_3 (refs. S2, S3). The Burstein−Moss shift experimentally observed for ITO is due to the conduction band occupancy as evidenced by the position of the Fermi level relative to the bottom of the conduction band[S2]. The dopant states in ITO do not exhibit significant localization at the Fermi level or conduction band minimum, implying

strong hybridization of dopant ions with coordinating oxygen ions. The main features of the band structure diagram remain similar for IMO. The Fermi level for IMO lies at lower energy relative to the conduction band minimum than that for ITO, consistent with the lower energy of LSPR band and a smaller Burstein−Moss shift. However, in contrast to ITO, Mo 4d states are localized around the Fermi level, which is consistent with anomalous Zeeman splitting of the excited conduction band states observed in the MCD spectra (Fig. 3e).

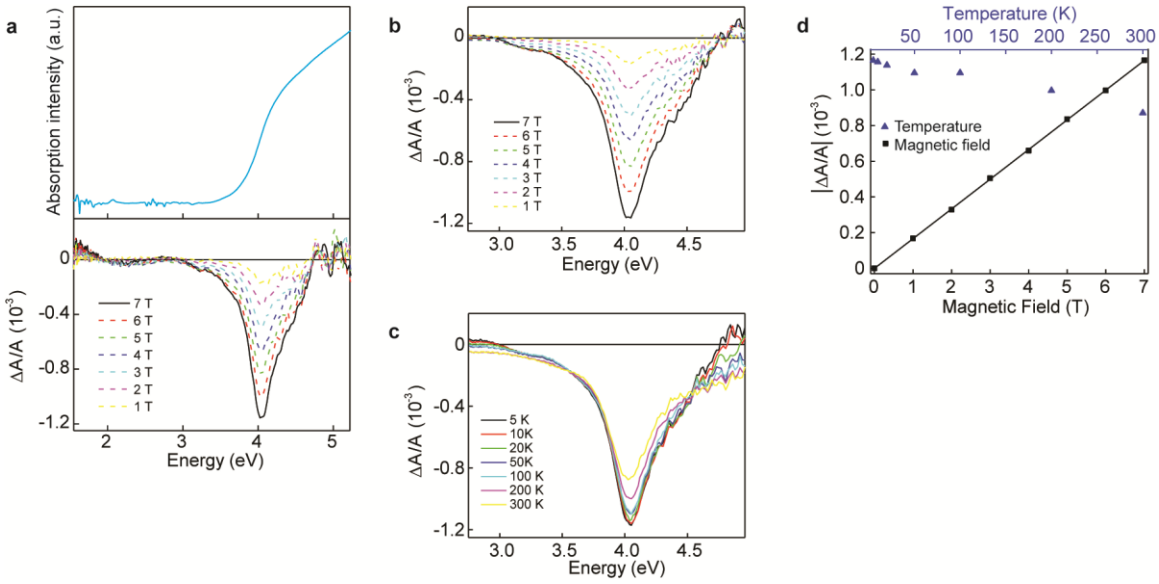

Supplementary Fig 8. Plasmon-induced band splitting in 9.2 % IMO nanocrystals. **a,** Absorption (light blue trace) and MCD (black and coloured dashed traces) spectra of 9.2 % IMO nanocrystals collected at 5 K. External magnetic field strengths corresponding to different MCD spectra are indicated in the graph; **b,** Exciton MCD spectra of 9.2 % IMO nanocrystals collected at different magnetic field strengths, as indicated in the graph; **c,** 7 T MCD spectra of 9.2 % IMO nanocrystals collected at different temperatures (5-300 K); **d,** Magnetic field (black squares) and temperature (blue triangles) dependence of MCD intensity recorded at the maximum of the negative MCD band for 9.2 % IMO nanocrystals. The MCD intensity follows linear dependence on the magnetic field associated with plasmon-exciton coupling, and slightly decreases with temperature, as expected from the Curie's law, owing to the presence of Mo^{5+}. These results reiterate the conclusions of the main text for IMO nanocrystals.

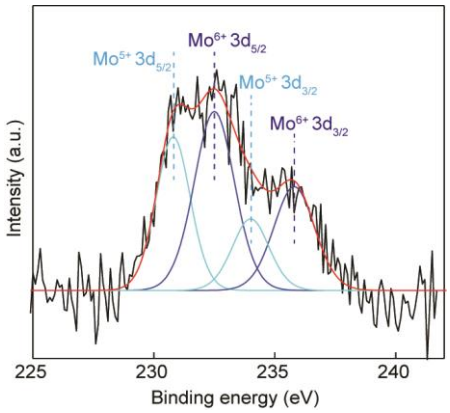

Supplementary Fig 9. Oxidation state of molybdenum in IMO nanocrystals. Molybdenum 3d XPS spectrum of typical IMO nanocrystals. The Gaussian peak fitting suggested the presence of molybdenum in Mo^{5+} and Mo^{6+} oxidation states. The peak assignments are indicated in the graph.

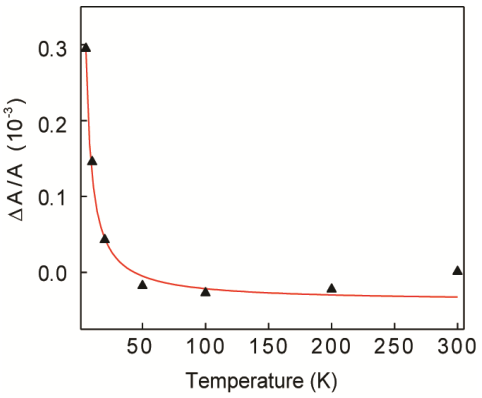

Supplementary Fig 10. Spin-induced splitting in IMO nanocrystals due to the presence of Mo^{5+}. Temperature dependence of the C-term MCD intensity for 0.3 % IMO nanocrystals, obtained by subtracting maximum MCD intensity at 300 K (A-term) from the maximum MCD intensities at other temperatures. Red line is the best fit to the experimental data using eq. 5 in Methods (Curie's law). The agreement of the experimental data with the Curie's law confirms the anomalous Zeeman splitting of the ground state in IMO nanocrystals induced by the paramagnetism due to the presence of Mo^{5+}.

Supplementary Text

The cyclotron motion of a free electron in solid state materials caused by an external magnetic field can also give rise to the formation of Landau states, which are associated with the Landau diamagnetism. It is therefore instructive to briefly compare and contrast the spectroscopic properties of the Landau states with those of the magnetoplasmonic modes observed in this work.

The Schrödinger equation for the cyclotron motion of free electrons in a magnetic field has a harmonic oscillator form[S4], with the characteristic angular rotation frequency (ω_c) of the harmonic oscillator expressed as:

$$\omega_c = \frac{eB}{m^* c} \qquad \text{(S1)}$$

where m^* is the effective mass of the carrier. The energy eigenvalues (known as Landau levels) for an electron in a parabolic band in a semiconductor are then given by:

$$E_{N,m_S} = \frac{\hbar^2 k_z^2}{2m_{\|}^*} + \hbar\omega_c\left(N + \frac{1}{2}\right) - g_S \mu_B m_S B \qquad \text{(S2)}$$

where $m_{\|}^*$ is the effective mass component along the magnetic field, k_z is the wave vector in the direction of the magnetic field, N is the Landau quantum number (N=0, 1, 2,…), and m_S is the magnetic spin quantum number ($m_S = \pm 1/2$). According to last term of eq. S2 each Landau level is split into two sublevels due to spin-orbit coupling determined by the Landé g factor (Supplementary Fig. 10a). This quantization of the Landau levels gives rise to a variety of magneto-oscillatory phenomena.

Importantly for this work, the interband (exciton) absorption transitions involving Landau levels obey the selection rule ΔN=0 (Supplementary Fig. 10a) [ref S5]. The transition energies for the corresponding MCD spectra in Faraday configuration for left ($h\nu_N^-$) and right ($h\nu_N^+$) circularly polarized light are defined as:

$$h\nu_N^{\mp} = E_g + \frac{\hbar^2 k_z^2}{2m_r^*} + \hbar\omega_c\left(N + \frac{1}{2}\right) \pm \frac{1}{2}\bar{g}\mu_B B \qquad \text{(S3)}$$

where E_g is the optical bandgap energy, m_r^* is the reduced effective mass of the bands and ω_c is the associated cyclotron frequency, and $\bar{g}$ is the combined *g*-factor of both bands. The dependence of transitions energies on *N* results in the periodic oscillatory structure of both absorption and MCD spectra (Supplementary Fig. 10b), which is a signature of the Landau level spectroscopy[S5]. Furthermore, the spin-orbit splitting of the Landau states shown in Supplementary Fig. 10a leads to both positive and negative MCD bands. As emphasized in the main text, in addition to robust MCD signal at high temperature (above 300 K) and low field (below 1 T), the absence of any periodic variations in either absorption or MCD spectra and the presence of only negative MCD signal at high temperatures demonstrate that carrier polarization in plasmonic semiconductor NCs reported in this work is associated with circular magnetoplasmonic resonance as a collective behaviour of free electrons.

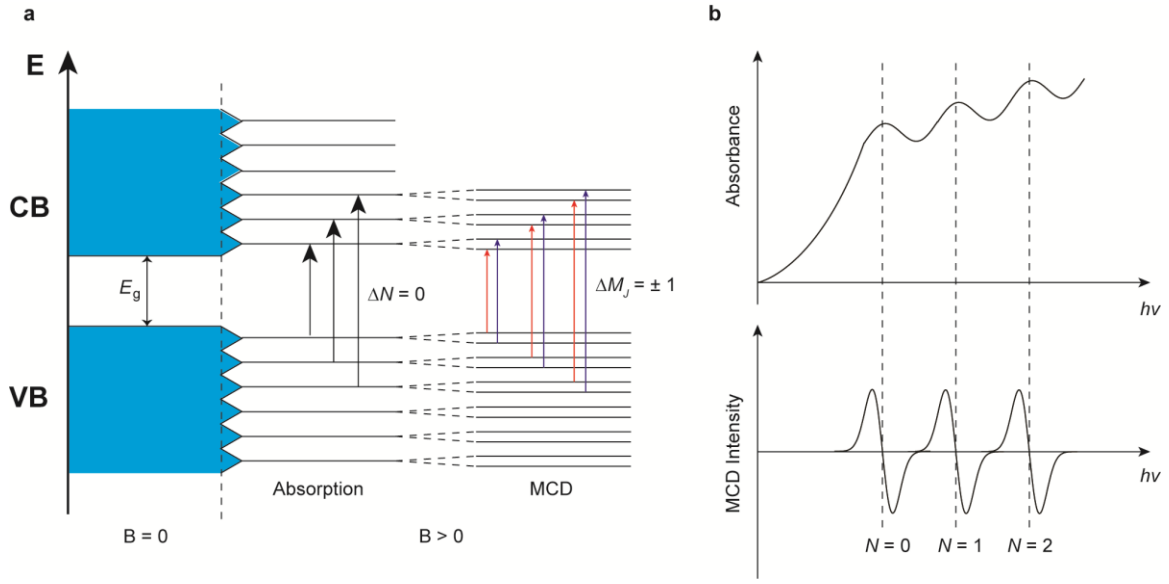

Supplementary Scheme 1. Landau level absorption and MCD spectroscopy. a, Schematic representation of the Landau levels for the valence band (VB) and the conduction band (CB) in an external magnetic field (*B*). Interband absorption and MCD transitions involving these Landau levels are shown with arrows; **b,** Exciton absorption (top part) and MCD (bottom part) spectra corresponding to the transitions indicated in **a**, which result in the characteristic oscillatory patterns.

Supplementary References

S1 Seidl, A., Görling, A., Vogl, P., Majewski, J. A. & Levy, M. Generalized Kohn-Sham schemes and the band-gap problem. *Phys. Rev. B* **53**, 3764-3774 (1996).

S2 Mryasov, O. N. & Freeman, A. J. Electronic band structure of indium tin oxide and criteria for transparent conducting behavior. *Phys. Rev. B* **64**, 233111 (2001).

S3 Chen, Z. *et al.* Electronic structures and transport properties of n-type-doped indium oxides. *J. Phys. Chem. C* **119**, 4789-4795 (2015).

S4 Dresselhaus, G., Kip, A. F. & Kittel, C. Cyclotron resonance of electrons and holes in silicon and germanium crystals. *Phys. Rev.* **98**, 368-384 (1955).

S5 Kessler, F. R. & Metzdorf, J. in *Landau level spectroscopy*: *Modern problems in condensed matter sciences* (eds G. Landwehr & E. I. Rashba) (Elsevier Science Publishers, Amsterdam, 1991).